



An experimental investigation of dynamic ice accretion process on a wind turbine airfoil model considering various icing conditions

Linyue Gao, Yang Liu, Hui Hu*

Department of Aerospace Engineering, Iowa State University, Ames, IA 50011-2271, United States

ARTICLE INFO

Article history:

Received 13 July 2018

Received in revised form 27 December 2018

Accepted 29 December 2018

Keywords:

Icing physics

Ice accretion process

Transient water runback

Surface temperature evolution

Wind turbine icing

Glaze ice

Rime ice

ABSTRACT

In the present study, the dynamic ice accretion process over a typical wind turbine airfoil model (i.e., DU96-W-180 airfoil) was experimentally investigated under various icing conditions. The experimental study was conducted in the Icing Research Tunnel of Iowa State University (i.e., ISU-IRT). Different icing conditions (i.e., rime, mixed and glaze) that wind turbine may experience in winter were reproduced by manipulating the airflow temperature, velocity, and liquid water content (LWC) in ISU-IRT. While a high-speed imaging system was used to reveal the dynamic ice accretion process over the surface of the test model, an infrared (IR) thermal imaging system was used to map the corresponding temperature distributions over the ice accreting airfoil surface. Time variations of the ice thickness accreted along the leading edge (LE) of the test model were extracted based on the acquired high-resolution images of the ice accretion process under different test conditions. It was found that, due to the obvious runback of the impacted water (i.e., formation of water film and rivulets) over the airfoil surface, the growth rate of the ice layer accreted along the airfoil leading edge was much slower under the glaze icing condition, in comparison with those under the rime and mixed icing conditions. Such surface water transport behavior was also found to expand the ice influencing region. From the temperature evolutions during the dynamic icing processes, the transient processes of droplet impingement, water film/rivulets formation, and ice roughness growth were temporally resolved, providing comprehensive details of the unsteady heat transfer during the dynamic icing process. While the surface temperature increment due to the direct droplet impingement was found to decrease monotonously along the chord in rime case, a stream-wise ‘plateau’ region was observed in the glaze and mixed icing cases due to the complex multiphase mass/heat transfer associated with the surface water transport behaviors.

© 2018 Published by Elsevier Ltd.

1. Introduction

Cold climate areas are usually promising sites for wind energy industries due to the abundant wind resources and low population density [1,2]. As a result, a plenty of wind farms have been built in the cold regions in North American, northern Asia and Europe. Due to the nature of cold temperature in these regions, wind turbine icing events are more likely to occur, which can cause serious performance degradation and shortened lifetime for wind turbines. Ice accretion on wind turbine blades can essentially alter the aerodynamic profiles of the blades, hence, degrade the aerodynamic performance of wind turbines (i.e., drag increase and lift decrease) [3,4]. Under severe icing conditions, wind turbines usually have to be shut down to avoid mechanical damages [5]. The downtimes due to wind turbine icing, which may last for days or weeks, can

lead to enormous economic loss for wind farm operators. In addition to the power output penalties, the uneven ice accretion along the wind turbine blade span can also cause edgewise vibrations, resonance, and unbalance loads, which may significantly shorten the lifespan of wind turbines [6,7]. Moreover, the secondary effects, i.e., increased noise and shedding of large ice chunk, are potential safety hazards for the nearby residents and running vehicles [8].

Ice accretion would occur when super-cooled water droplets impact onto the surfaces of wind turbine blades with tremendous latent heat of fusion being released associated with the solidification (i.e., phase change) process of the impacted super-cooled droplets. The freezing of the impacted water mass can be complete or partial, depending on how rapidly the latent heat of fusion can be released into the ambient air. Rime ice usually forms at the very cold temperatures when the impinged water droplets freeze immediately upon impacting on wind turbine surfaces. Glaze ice usually forms at relatively warm conditions (i.e., temperatures just

* Corresponding author.

E-mail address: huhui@iastate.edu (H. Hu).

Nomenclature

Latin symbols

C	chord length
D	characteristic length
F_d	aerodynamic force
F_c	capillary force
F_{cen}	centrifugal force
A_c	ice accumulation parameter
L	span-wise averaged length
P	pressure
Q	adiabatic heat flux
r	blade radius position
R	blade length
t	freezing time
T	temperature
V	stream-wise velocity
X, Y, Z	span-wise coordinate, stream-wise coordinate, vertical direction coordinate

Greek symbols

α	icing rate (ice thickness upon the leading edge)
β	time derivation of A_c
ρ	density

Abbreviations

AoA	angle of attack
IEA	International Energy Agency

IR	infrared
ISU-IRT	Icing Research Tunnel at Iowa State University
LE	leading edge
LF	linear fitting
LWC	liquid water content
MVD	median volumetric diameter
RPM	revolutions per minute
RTV	relative temperature variation
TE	trailing edge
2D, 3D	two-dimensional, three-dimension

Subscripts

adh	adiabatic
cd	conduction
cv	convective
$evap$	evaporation
f	denotes ice film
i	denotes ice
LE	denotes leading edge of the airfoil model
lh	latent heat of solidification
kin	kinetic
ss	sensible
sub	sublimation
rad	radiation
r	denotes ice rivulets
∞	denotes oncoming flow conditions

below zero), in which case the impacted water mass would only freeze partially, while the remaining water would coalesce into films/rivulets and run back over the airfoil surface [1]. The transition/intermediate status between rime ice and glaze ice is usually called mixed ice. In comparison with rime ice, the wet nature of the mixed and glaze ice contributes to the formation of very irregular ice shapes, making the ice accreting processes being much more complicated [9–11].

Over the past decades, many studies have been performed to investigate the underlying physics pertinent to aircraft-icing phenomena [12–14]. Though the findings derived from these studies are very helpful to improve our understanding about wind turbine icing phenomena, many particular issues related to wind turbine icing have not been properly considered. For example, the optimized airfoil shapes used to design wind turbine blades usually have much greater airfoil thickness and blunter leading edge, in comparison with those used in aircraft wing design. Wind turbine blades usually have very different surface properties (e.g., roughness, wettability and thermal conductivity) in comparison with those of airframe, which can significantly affect the dynamic ice accretion process [15]. In addition, wind turbines are usually operated at much lower altitude (i.e., closer to sea level), and more prone to encounter freezing rain and other low altitude, high-liquid-water-content environments (such as ocean spray). Therefore, it is highly desirable to gain a keen understanding of the underlying physics pertinent to wind turbine icing phenomena.

In the present study, a comprehensive investigation was conducted to examine the dynamic ice accretion process over the surface of a typical wind turbine blade/airfoil model under various icing conditions (i.e., rime, mixed and glaze). The experimental study was performed in the Icing Research Tunnel available at Iowa State University (i.e., ISU-IRT). In the sections that follow, while the fundamental mechanisms of wind turbine icing is

illustrated at first, the experimental setup and test model used in the present study are described in great details. Then, based on the experimental results of dynamic ice accretion processes, ice impact regions and surface temperature distributions under the different icing conditions, further discussions are given to provide more insights of the underlying physics in the complex ice accretion process on the wind turbine blade/airfoil model.

2. Fundamental mechanisms of ice accretion on wind turbine blade/airfoil surface

Fig. 1 shows the schematics of the framework to analyze the dynamic ice accretion process over the surface of a typical wind turbine blade. As shown in Fig. 1(a), an arbitrary control volume is selected over the airfoil surface to analyze the heat transfer process during the dynamic ice accretion process. Based on the energy conservation law [16], the energy balance within the control volume at the thermal equilibrium state can be summarize as Eq. (1).

$$Q_{lh} + Q_{adh} + Q_{kin} + Q_{ss} = Q_{sub} + Q_{evap} + Q_{cd} + Q_{cv} + Q_{rad} \quad (1)$$

where Q_{lh} is the latent heat of fusion, Q_{adh} is the adiabatic heat, Q_{kin} is the kinetic heat, Q_{ss} is the sensible heat, Q_{sub} is the sublimation heat, Q_{evap} is the evaporation heat, Q_{cd} is the conductive heat, and Q_{cv} is the convective heat.

During the icing process, the latent heat of fusion would be released as the impacted super-cooled water droplets freeze (i.e., solidification) over the airfoil surface, which is the main source of the surface temperature increment. Another source of energy input is from adiabatic heating which is caused by air friction. It should be noted that the kinetic energy brought by the impinging water droplets also contributes to the surface temperature increment. The heat in the control volume would be mainly dissipated

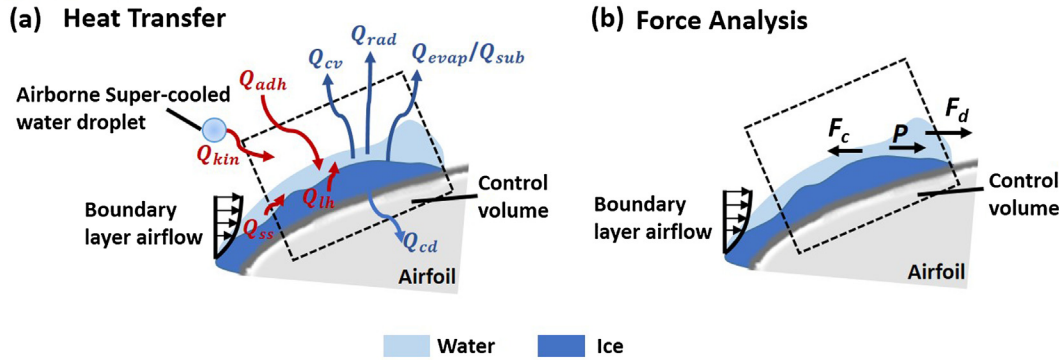


Fig. 1. Icing mechanism on a wind turbine blade/airfoil. (a) Heat transfer; (b) Force analysis.

by heat transfer that includes both convective and conduction heat transfer processes. While the convective heat transfer is caused by the temperature difference between the water/ice layer and the incoming airflow, the conductive heat transfer is due to the temperature gradient within the water/ice layer and the model substrate. A small amount of heat loss is also caused by sublimation of ice and evaporation of water. For the energy balance in the control volume, the release of latent heat of fusion and the convective/conductive heat transfer are the dominant mechanisms of the energy input and output, respectively. In comparison with the traditional metal-based aircraft wings, the thermal conductivity of the polymer-composite-based wind turbine blades is much lower (i.e., $<0.5\text{--}1.0\text{ W/m K}$ for wind turbine blade vs. $\sim 200\text{ W/m K}$ for metal-based aircraft wings). Therefore, while the icing process over the surface of polymer-composite-based wind turbine blades is mainly affected by the convective heat transfer, the ice accretion over the metal-based aircraft wing is determined by both the convective heat transfer and conductive heat transfer.

In rime icing conditions, the impacted water droplets freeze instantly with no water transport over the surfaces. However, under glaze icing conditions, the unfrozen water mass would form into films/rivulets with bulge shapes, which could provide a comparatively large aerodynamic drag to overcome the resistance of capillary force, thereby, push the water mass transport to further downstream over the airfoil surface [17]. Fig. 1(b) shows the neutral equilibrium between capillary force caused by surface tension, F_c , aerodynamic force, F_d , and water static pressure, P , of the film/rivulet flows over ice structures in the steady state. In the neutral equilibrium, capillary force equals to the sum of aerodynamic drag and water static pressure, i.e., $F_c = F_d + P$ [18]. The magnitude of the forces acting on film/rivulet flows is essentially determined by the airfoil geometry and incoming airflow conditions. In comparison with the airfoils used for aircraft wings, wind turbine dedicated airfoils are usually asymmetric and cambered with larger thicknesses to ensure sufficient structural strengths. Such unique features of the wind turbine airfoil are suggested to have great influences on the aerodynamic forces exerted on the impacted water droplets, and thereby the dynamic ice accretion processes over the wind turbine blade surfaces.

3. Experimental setup and tested wind turbine airfoil model

The experimental study was performed in the Icing Research Tunnel available at Aerospace Engineering Department of Iowa State University (i.e., ISU-IRT). The icing research tunnel, as schematically shown in Fig. 2, has a test section of 2.0 m in length \times 0.4 m in width \times 0.4 m in height with four optically transparent panels. ISU-IRT has a capacity of generating a maximum wind speed of 60 m/s and a minimum airflow temperature of

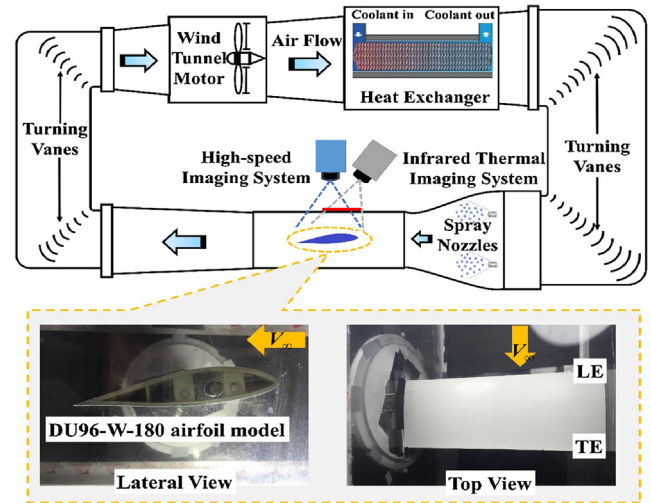


Fig. 2. Schematic diagram of experimental setup for icing physics study over DU96-W-180 airfoil model.

$-25\text{ }^\circ\text{C}$. An array of eight pneumatic atomizer/spray nozzles were installed at the entrance of the contraction section to inject micro-sized water droplets ($10\text{--}100\text{ }\mu\text{m}$ in size) into the airflow. By manipulating the flowrate through the spray nozzles, the liquid water content (LWC) in ISU-IRT could be adjusted within a wide range from 0.1 g/m^3 to 10.0 g/m^3 . Therefore, ISU-IRT is capable to simulate atmospheric icing phenomena over a wide range of icing conditions (i.e., from dry rime to extremely wet glaze ice conditions) [10,11,19].

The airfoil model used in the present study was designed based on the DU series airfoil, DU96-W-180. This airfoil profile has been widely used for the design of outboard sections on wind turbine blades ascribe to its high lift-to-drag ratio, insensitivity to roughness, and low noise [20,21]. DU96-W-180 airfoil is a low-speed, asymmetric and cambered airfoil with a thickness-to-length ratio of 0.18. The polymer-composite-based airfoil model was produced by using a rapid prototyping machine (i.e., 3D printer). The chord-wise and span-wise dimensions of the airfoil model are 152.4 mm and 400 mm, respectively. The surface of the airfoil model was coated with the protective spray-on enamel (Rustoleum™, Protective Enamel, white in color) and then wet-sanded by using up to 2000 grit sandpapers to ensure sufficient surface smoothness. Fig. 2 shows the lateral view and top view of the test model mounted at its quarter-chord across the middle of the test-section of ISU-IRT. Three stainless steel rods were used to support the model. The airfoil model can be pivoted to the desired angles of attack (AoA) by using a digital inclinometer.

As shown in Fig. 2, while a high-speed imaging system was utilized to capture the dynamic icing process over the airfoil surface, an IR thermal imaging system was used simultaneously to quantitatively measure the corresponding surface temperature distributions over the airfoil surface. The two systems were synchronized and triggered by using a digital delay/pulse generator (BNC, Model 577). The high-speed camera (PCO Tech, Dimax) was installed right above the test model with a 24 mm lens (Nikon, 24 mm Nikkor 2.8D), providing a top view of 1600×888 pixels with a resolution of 5.08 pixels/mm. The IR system was composed of an IR camera (FLIR, A615) and an IR inspection window (FLIR, IR Window-IRW-4C). The IR camera, which can detect waves within a range of 7.5–14 μm , was mounted above the test model, providing a field of view of 640×480 pixels with a resolution of 4.77 pixels/mm. The IR inspection window was embedded in the top panel of the test section. The emissivity values of water, ice and the airfoil surface coated with protective enamel (white in color) are 0.95–0.96, 0.96–0.98 and 0.96, respectively [13,22]. Since the emissivity values of these materials are very close with a difference less than 3%, the uncertainty of the measured surface temperature caused by emissivity is suggested to be very small and negligible. During the experiments, a high-accuracy thermocouple was also integrated over the surface of the airfoil model to provide in-situ calibration of the surface temperature measurements by the IR system.

4. Case study

4.1. Case design

In order to investigate the dynamic ice accretion processes under different icing conditions, we conducted a series of icing experiments covering a wide range of real icing conditions with respect of ambient air temperature, incoming airflow velocity, liquid water content (LWC) and median volumetric diameter (MVD). While the MVD was controlled in a range of 20–30 μm to simulate the impinging water droplets onto the wind turbine blades in real field environments [23,24], different ambient air temperatures (i.e., -5°C , -10°C , and -15°C), incoming airflow velocities (i.e., 20 m/s, 30 m/s, and 40 m/s), and LWC levels (i.e., 0.3 g/m^3 , 1.1 g/m^3 , 3.0 g/m^3) were used for the case design in the present study.

Table 1 lists the representative cases to be discussed in the following sections. It should be noted that, while the air temperature was kept at -10°C for all cases, the AoA was also kept at 5° , at which the airfoil model possesses the maximum lift-to-drag ratio as suggested by Timmer and van Rooij [21]. The airfoil profile of DU96-W-180 is usually applied at 60–99% span-wise positions, where the relative velocity ranges approximately from 25 m/s to 80 m/s for a 1.5-MW wind turbine. Therefore, the velocity of the oncoming airflow was set to be 40 m/s to represent the typical relative velocities in real situations. The Reynolds number in the present study is 4.2×10^5 , which is smaller than that of real wind turbine blades (i.e., usually operated at the Reynolds number of 10^6). However, the previous study [25] has demonstrated that the effects of Reynolds number on the aerodynamic performance of such DU airfoils are very small in comparison to the NACA airfoils. Since wind turbines are usually operated at very low altitude in comparison with aircraft, they are more prone to encounter

high-water-content conditions (e.g., freezing drizzle/rain and ocean spray). The LWC level for wind turbine icing usually ranges from 0.1 to 5.0 g/m^3 , which is much higher than that of aircraft in-flight icing conditions ($<1.0 \text{ g/m}^3$) [26]. In the present study, various LWC values (i.e., 0.3 g/m^3 , 1.1 g/m^3 , 3.0 g/m^3) were modulated to achieve different icing conditions as suggested in Appendix C [27].

4.2. Identification of ice types

Snapshots of ice accretion on the airfoil model (i.e., after 300-s ice accretion) obtained from the high-speed imaging results are shown in Fig. 3 to further identify the ice types formed in the different test cases. The formation of runback rivulets is the most evident feature to distinguish rime ice and glaze ice. The isolated rivulets shown in Case No. 3 indicate a typical glaze ice accretion. While no obvious rivulet formation can be seen in Case No.1 and Case No. 2, the different appearances of the ice structures shown in these two cases provide evidences in identifying the rime ice formation in Case No. 1 (i.e., milky ice layer with crystalline structures) and the mixed ice formation in Case No. 2 (i.e., clear icicles stand on the surface towards the oncoming flow direction) [27].

5. Results and discussion

5.1. Demonstration of centrifugal effects on the icing process over a wind turbine blade

The tip region of a wind turbine blade captures the most wind energy. Meanwhile, due to the larger local droplet impact velocity, more ice would accrete at the tip region of the turbine blade. There are mainly two dominating forces acting on a droplet impacting onto a wind turbine blade, i.e., aerodynamic force (F_d) vs. centrifugal force (F_{cen}). While the centrifugal force (F_{cen}) of the impacting droplet would increase linearly as a function of the blade radius location of the impacting droplet (i.e., $F_{cen} = m\omega^2r$, where m is the mass of the droplet, ω is and rotational speed of the rotor, and r is the radius position of the blade), the aerodynamic force (F_d) would also increase at the outer sections of the wind turbine blade. In the present study, a comparison between the centrifugal force (F_{cen}) and aerodynamic force (F_d) was first conducted to demonstrate the impact of centrifugal force on the icing process over wind turbine blades.

The span-wise variation of the ratio between centrifugal force and aerodynamic force (i.e., F_{cen}/F_d) was estimated based on technical parameters of the NREL 5 MW reference wind turbine, and the results are plotted in Fig. 4(a). If the size of the supercooled water droplets is small (i.e., 20 μm in diameter as used in the present study), the ratios of centrifugal force to aerodynamic force are quite small at all span positions, indicating that the effects of centrifugal force on the dynamics of the airborne droplets is negligible. If the size of the water droplets is very large (e.g., 200–500 μm in diameter), while the ratio of the centrifugal force to aerodynamic force would increase; however, it is still less than 5% in the tip region. The estimated ratio of centrifugal force to aerodynamic force derived in this study can be validated by the ice accretion images shown in Fig. 4(b), which were taken from the field measurements

Table 1
Representative cases for icing physics study on DU96-W-180 airfoil model.

Case No.	AoA [$^\circ$]	V_∞ [m/s]	T_∞ [$^\circ\text{C}$] (± 1.5)	LWC [g/m^3]	Expected Ice type
1	5	40	-10	0.3	Rime
2	5	40	-10	1.1	Mixed
3	5	40	-10	3.0	Glaze

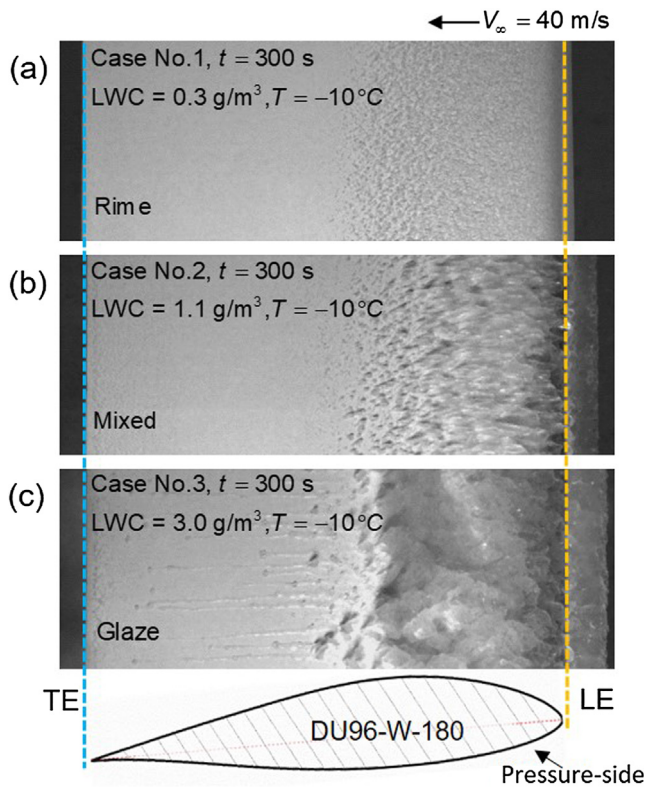


Fig. 3. Snapshots of ice accretion over the pressure-side surface of DU96-W-180 airfoil model in representative cases for identification of ice types. LE and TE help pinpoint the spatial scale.

of Shu et al. [28] on a real wind turbine with environmental conditions of Relative Humidity $RH = 100\%$, temperature $T = -3.5\text{ }^\circ\text{C}$, incoming airflow velocity $V_\infty = 7.8\text{ m/s}$ (at the hub height) and after 6 hours of ice accretion time [28]. It is clearly seen that, while the ice accretion over the root region has evident span-wise features, the ice structures accreted over the mid-span and tip regions are essentially along the chord-wise direction. Therefore, centrifugal effects on the icing process over a wind turbine blade, especially in the outer regions of turbine blades, are negligible. Therefore, the experimental setup in the present study can be used to study the icing physics pertinent to wind turbine icing phenomena.

5.2. Full life cycle of the dynamic icing process over a wind turbine blade

Fig. 5 shows the snapshots of the dynamic icing process over the airfoil surface under rime, mixed and glaze icing conditions at different ice accretion moments. Fig. 5(c) shows the dynamic icing process under the glaze icing condition. Three stages of the glaze icing process are extracted: water droplets impingement, rivulet formation and ice accretion along the leading edge. In the first stage, the super-cooled water droplets carried by the oncoming airflow impinge onto the region near the LE of the test airfoil model and the wind-driven surface water quickly forms into a thin water film that advances further downstream. During this process, the thickness of the water film decreases as it transports downstream. When the thickness of water film achieves the minimum limitation (i.e., defined as a function of surface tension and shear stress) at the water/air interface as given in Al-Khalil et al. [29], the film front would split into isolated water rivulets, indicating the start of the second stage (see Fig. 5(d) snapshot1). While the water rivulets move downstream, the convective heat transfer would take away the remaining latent heat of fusion in the runback water [18,30], generating the rivulets-shaped ice formation as can be observed in the snapshot at $t = 80\text{ s}$. Then, the icing process comes into the third stage. The icicles start to build up towards the LE with most of the impinged water droplets collected and frozen along the LE. As the icicles grow, they merge into the cusp-like tops (see Fig. 5 (d) snapshot2). More apparent features caused by the volume expansion during the icing process [31] are shown in the mixed icing case, as shown in Fig. 5(b). Only two stages exist in mixed icing condition, water droplet impingement and ice accretion. An expansion of the thin water/ice film is observed at $t = 20\text{ s}$. The front of the film appears to be serrated without obvious rivulet formation (see Fig. 5(d) snapshot3). During the ice accretion process, feather-like icicles are formed towards the LE of the airfoil model (see Fig. 5(d) snapshot4). Compared to the mixed ice accretion, the ice layer formed in the rime icing case has a milky appearance with crystalline structures (see Fig. 5(d) snapshot5), as shown in Fig. 5(a). It should be noted that, while the ice accretion features revealed above would be representative of most typical icing scenarios over the surfaces of wind turbine blades, the actual morphologies of ice structures accreted over turbine blade surfaces would be affected by many contributing factors, including ambient temperature, LWC level, wind speed, the ice accretion duration as

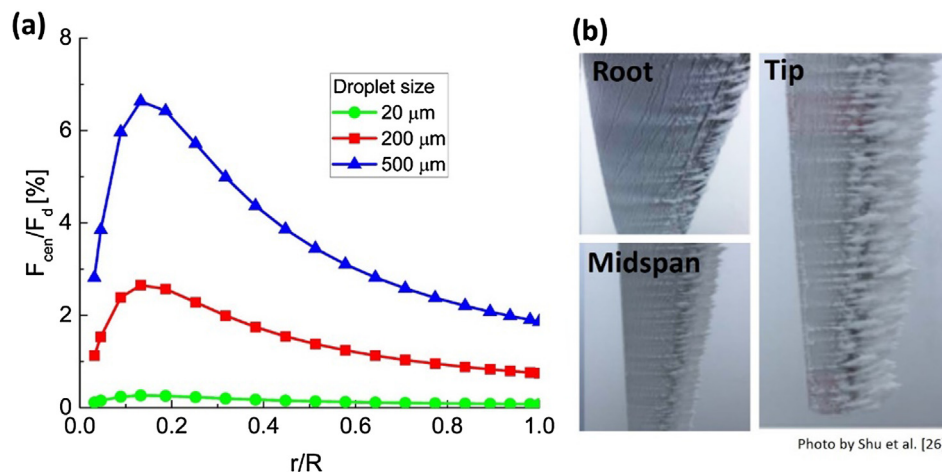


Fig. 4. Impact of centrifugal force on the icing process. (a) Estimated ratio of centrifugal force to aerodynamic force acting on a droplet as a function of normalized blade radius positions by blade length. (b) Photos of ice accumulation on different regions of a wind turbine blade [28].

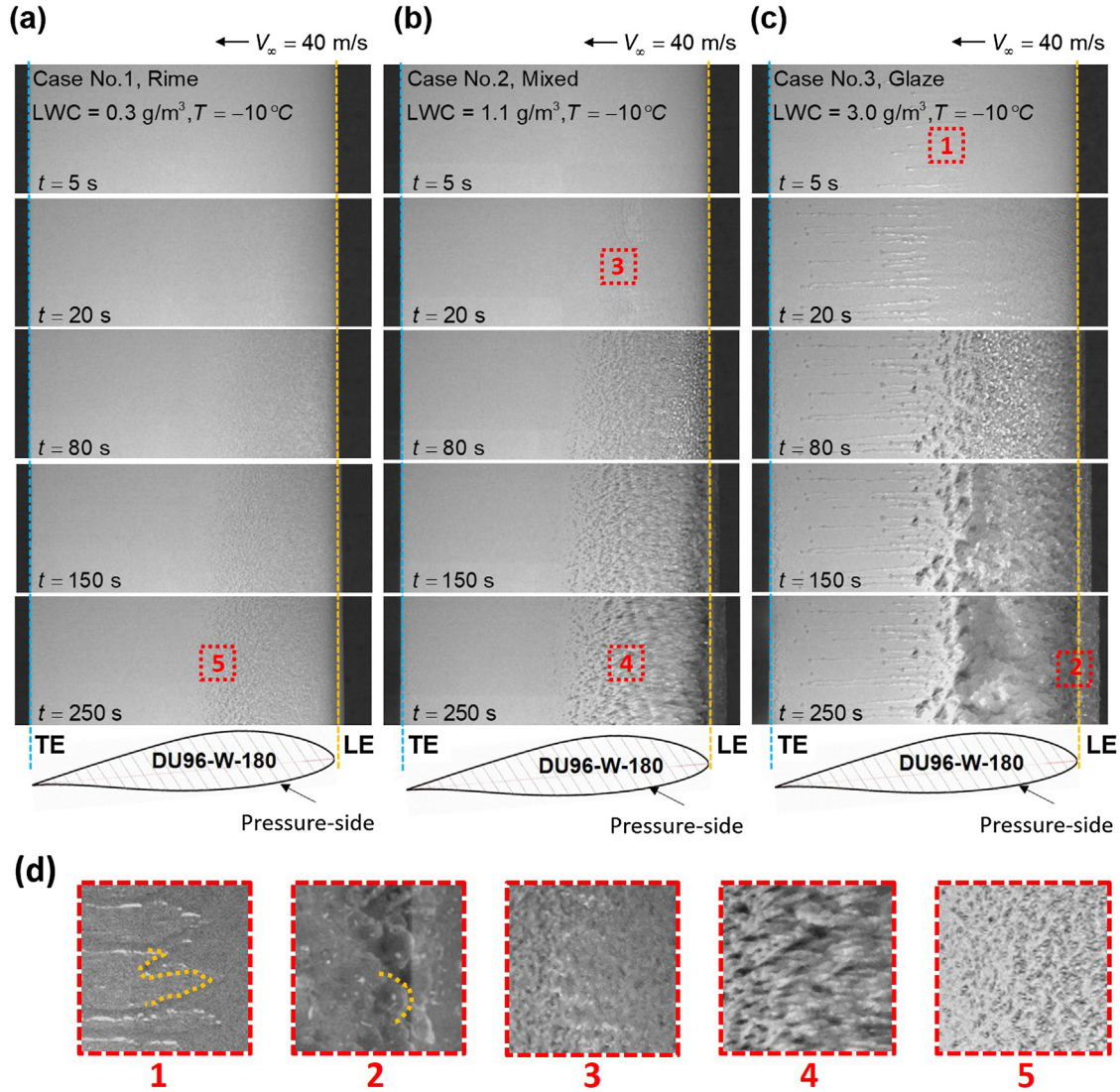


Fig. 5. Snapshots of dynamic ice accretion process over the pressure-side surface of DU96-W-180 airfoil model under various icing conditions. Red squares highlight the zoomed areas. (a) Rime icing; (b) Mixed icing; (c) Glaze icing; (d) Zoomed snapshots. The contrasts of the zoomed snapshots were adjusted to provide a clearer view. (For interpretation of the references to color in this figure legend, the reader is referred to the web version of this article.)

well as the centrifugal force induced by the rotation of the turbine blades as reported in Shu et al. [28].

5.3. Quantification of icing impacted regions

5.3.1. Parameter definitions of icing impacted regions

Three icing impacted regions are highlighted according to the full life-cycle icing accretion process. The quantification of these regions can give not only a more explicit understanding of the icing process, but also a constructive reference for optimization of resistant heater installation for wind turbine icing mitigation.

Fig. 6 shows three ice impacting regions. The first region is the ice film. L_f represents the stream-wise length of the ice film, determined by the span-wise-averaged distance from the leading edge to the contacting line of ice film/rivulet. The second region is ice rivulet, which only occurs in glaze icing conditions. L_r is the span-wise-averaged length of ice rivulets, calculated by using Eq. (2). Three special configurations of ice rivulets are shown in snapshots and Fig. 6(b) shows the calculation method for them. If a large gap exists in one rivulet with a small downstream part (see Type 1), L_r is defined as the length of upstream part. If the

ice rivulet splits into several branches (see Type 2), every branch is considered as one rivulet. If the ice rivulet does not appear in the snapshots completely (see Type 3), the length of it will not be counted. Notably, when the icing process comes into the third stage, the lengths of films/rivulets becomes more stable due to the solidification (i.e., freezing) of the water films/rivulets. The third region is ice accretion concentrated along the LE of the airfoil model. L_{LE} is the span-wise-averaged thickness of ice accretion along the LE. The boundary line of ice in front of the test model is extracted by using the method given in Waldman et al. [10]. The difference in snapshot intensity caused by the existence of water/ice are calculated by comparing the changes between the time sequences of snapshots with the initial reference. L_{LE} is then determined by the span-wise-averaged distance between the boundary line and leading edge.

$$L_r = \frac{\sum_{i=1}^n L_{r(i)}}{n} \tag{2}$$

where $L_{r(i)}$ is the length of i^{th} rivulet and n represents the total number of rivulets shown in the snapshots.

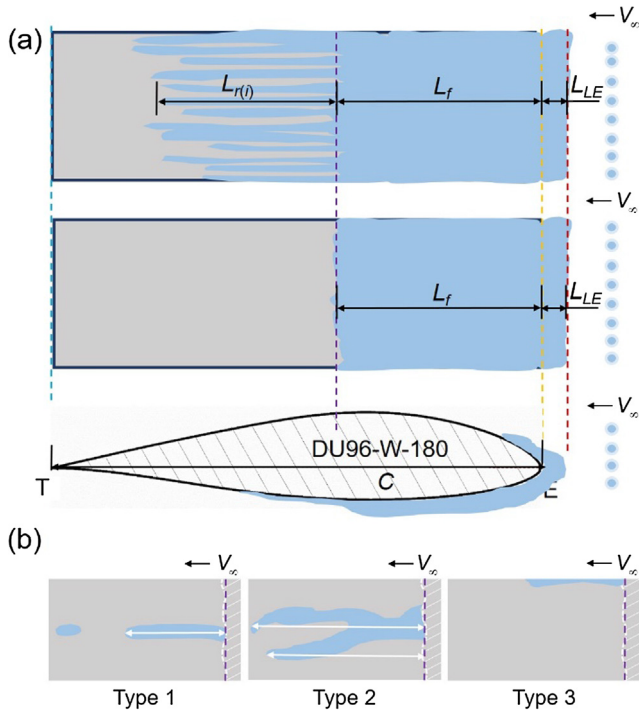


Fig. 6. Schematic diagram of dimensional parameters of icing impacting regions. (a) Definitions of parameters; (b) Calculation method for three special types of ice rivulets.

5.3.2. Length of ice film and length of ice rivulet

Fig. 7 compares the normalized lengths of ice films/rivulets after 250-s of ice accretion under rime, mixed and glaze icing conditions. The length of ice film is approximately 40% of chord length (C) for all cases. The dimension of ice film could be influenced by the following factors: (1) the properties of the test model, including geometric configurations, mounting angles, etc., which greatly determines the impinging area; (2) the environmental factors, including LWC level, ambient temperature, oncoming flow velocity, etc., which determines the freezing rate. The ambient temperature of these three cases is $-10\text{ }^\circ\text{C}$, a relatively low temperature at

which the water film can freeze rapidly with a very small expansion, which explains the similar results in the ice film length. The span-wise-averaged length of fifteen ice rivulets (highlighted by red dots in snapshots) and the cumulative length of ice film and rivulets are 36.6% C and 78.5% C, respectively.

5.3.3. Dynamic ice accretion at the airfoil leading edge

Fig. 8 shows the time histories of the ice thickness variations at the airfoil LE under three typical ice accretion conditions. As the time goes on, the normalized ice thickness increases correspondingly. At the beginning, nonlinear phenomena occur in both mixed and glaze icing cases due to the water runback over the airfoil surface. After that, the ice growth is found to become linear. The straight lines in Fig. 8 are the linear fitting results with their slopes representing the growth rate of leading-edge ice thickness, α , as defined by Eq. (3).

$$\alpha = \frac{d(L_{LE}/C)}{dt} \tag{3}$$

The ice accumulation parameter, A_c , as defined by Anderson [32], is given in Eq. (4)

$$A_c = \frac{LWC \cdot V_\infty \cdot t}{D \cdot \rho_i} \tag{4}$$

where D is the characteristic length and ρ_i is the density of ice. The time derivative of the ice accumulation parameter can be used to estimate the growth rate of the ice layer accreted over the airfoil surface, that is,

$$\beta = \frac{dA_c}{dt} = \frac{LWC \cdot V_\infty}{D \cdot \rho_i} \tag{5}$$

Since the variation of ice density is relatively small under the different icing conditions [33], as the incoming air flow velocity is kept the same, the growth rate of ice accretion would be proportional to the LWC level. In the present study, while the LWC in the rime, mixed, and glaze conditions was set to be 0.3 g/m^3 , 1.1 g/m^3 , and 3.0 g/m^3 , respectively, the ratio of total ice growth rate between the different ice types, i.e., β_{mix}/β_{rime} and $\beta_{glaze}/\beta_{mix}$, should have a similar value of ~ 3.0 , as estimated using Eq. (5). It has been demonstrated that the growth of leading-edge ice thickness, α , is a good indication of the growth of ice accretion over the airfoil surface if

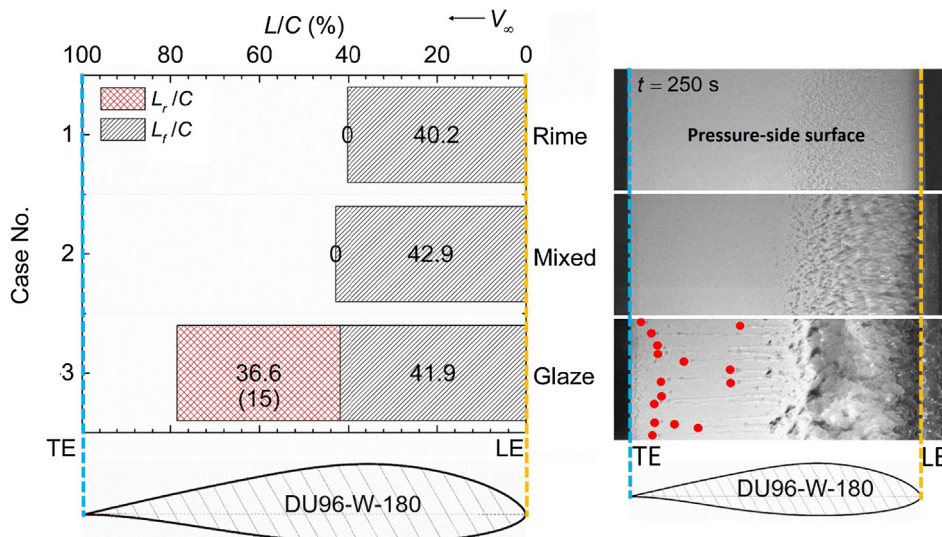


Fig. 7. Normalized lengths of ice films, lengths of ice rivulets and numbers of ice rivulets shown in the high-speed images under rime, mixed and glaze icing conditions when $t = 250\text{ s}$. The red dots in the snapshot point out the fifteen ice rivulets. (For interpretation of the references to color in this figure legend, the reader is referred to the web version of this article.)

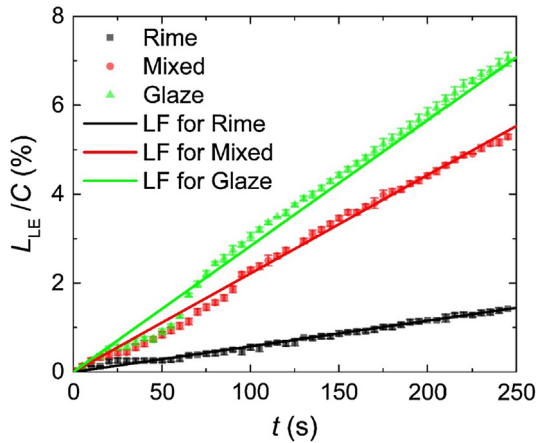


Fig. 8. Time series of the normalized thickness of ice accretion upon the LE and their linear fitting (LF) curves under rime, mixed and glaze icing conditions within the first 250 s. The error bar presents ± 1 standard deviation around the mean.

all of the impinged water droplets are frozen and accumulated around the LE region [34]. In the present study, since the ice accretion in the rime and mixed cases are mostly concentrated around the LE, the ratio of the LE ice thickness growth rate (as given in Fig. 9) is estimated to be $\alpha_{mix}/\alpha_{rime} = 3.2$, which agrees well with the estimated ratio of total ice growth rate, $\beta_{mix}/\beta_{rime} = 3.0$. For the glaze condition, however, since the impinged water droplets would not only freeze around the LE, but also runback over the airfoil surface driven by the boundary layer airflow, the ratio of the LE ice thickness growth rate between the glaze and mixed conditions is found to be much smaller, i.e., $\alpha_{glaze}/\alpha_{mix} = 1.3$, in comparison to the estimated ratio of total ice growth rate, i.e. $\beta_{glaze}/\beta_{mix} \sim 3.0$.

5.4. Time evolution of the surface temperature during the icing process

Unsteady heat transfer takes place during the dynamic icing process. The surface temperature contours give an index to the unsteady heat transfers and provide a more elaborate view of the icing process. Fig. 9 compares the temperature contours under rime, mixed and glaze icing conditions at six typical icing moments. From $t = 2$ s to $t = 15$ s, the area of high-temperature region undergoes the process of expanding for all of the three cases. In the rime case, no clear boundary lines can be observed

as those in the mixed and glaze icing cases. After the super-cooled water droplets impacted onto the surface of the test model near the LE, they immediately freeze over the test model surface, forming a thin ice layer. The latent heat of fusion released in this process results in a rapid temperature rise, also called recalescence [35], as shown in Fig. 9(a). As the time goes by, the temperature slightly increases and comes into a steady state. The temperature distribution along the chord monotonically decreases because less water droplets can be captured in the downstream region. In the mixed icing case, partial freezing of the impinged water droplets results in a water layer remaining over the ice layer, as shown in Fig. 9(b). While a portion of latent heat is conducted through the ice/surface interface or ice/water interface, most of the latent heat of fusion in the water layer is dissipated into the airflow by heat convection. In the glaze icing case, the much larger amount of water collected over the airfoil surface leads to a faster expansion. The rudiment of rivulets can be seen at $t = 2$ s in Fig. 9(c). At $t = 4$ s, obvious rivulets are stretched downstream beyond 0.5 C. It should be noted that, the temperature distribution over the ice accreting airfoil surface is not monotonous under the glaze icing condition. A region with relatively low surface temperatures is observed inside the icing impacted area.

Fig. 10 shows the stream-wise surface temperature variations at the first ~ 10 s of ice accretion experiment. While ΔT is defined as the temperature change during the dynamic icing process, Y/C is the normalized stream-wise location on the airfoil surface. In the rime icing case, the impinged water droplets freeze immediately upon impacting onto the airfoil surface and the ice mass varies monotonously with respect to the water collection efficiency [19]. The temperature variation ΔT has a peak around the leading edge, i.e., the direct impinging area, due to the maximum local water collection efficiency. The water collection efficiency decreases gradually at the further downstream, which is caused by the geometric configuration and the AoA of the airfoil model. As the time goes by, the ‘peak’ ΔT increases gradually and then becomes stable. Other cases have the similar trends with shorter time duration to reach the steady state. The larger amount of water droplet impingement in the mixed and glaze icing cases leads to the formation of surface water runback over the ice accreting airfoil surface, which affects the heat transfer process and results in a ‘plateau’ region in the surface temperature distributions. In the glaze icing case, the ‘plateau’ region moves downstream slightly as the time goes by due to the stretching of water film. While the continuous water droplet impingement supplements the

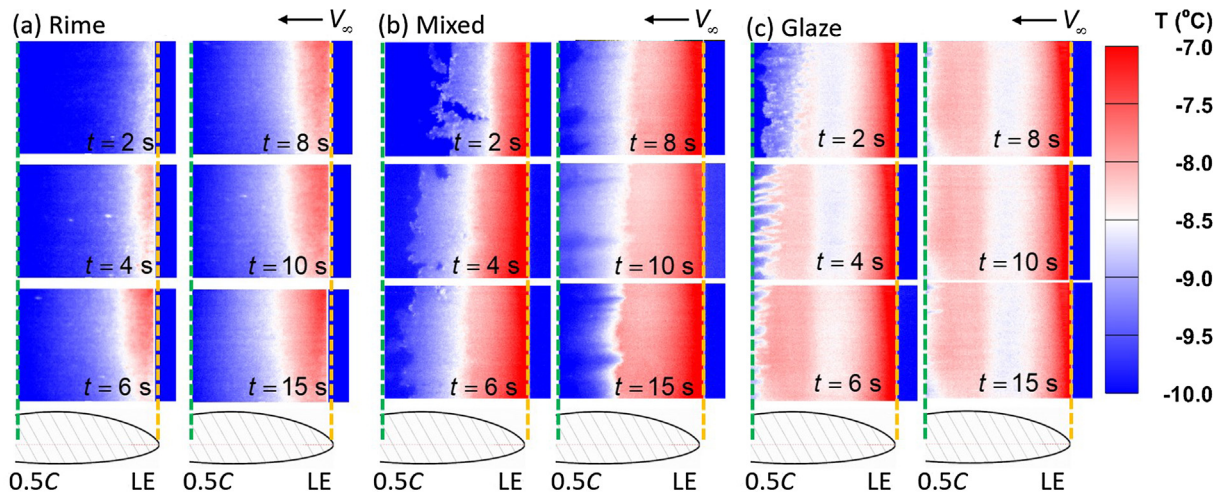


Fig. 9. Contours of surface temperature distribution over the pressure-side surface of DU96-W-180 airfoil model under (a) rime icing, (b) mixed icing and (c) glaze icing conditions. Noted that the surface temperature represents the temperature of the top layer of the medium.

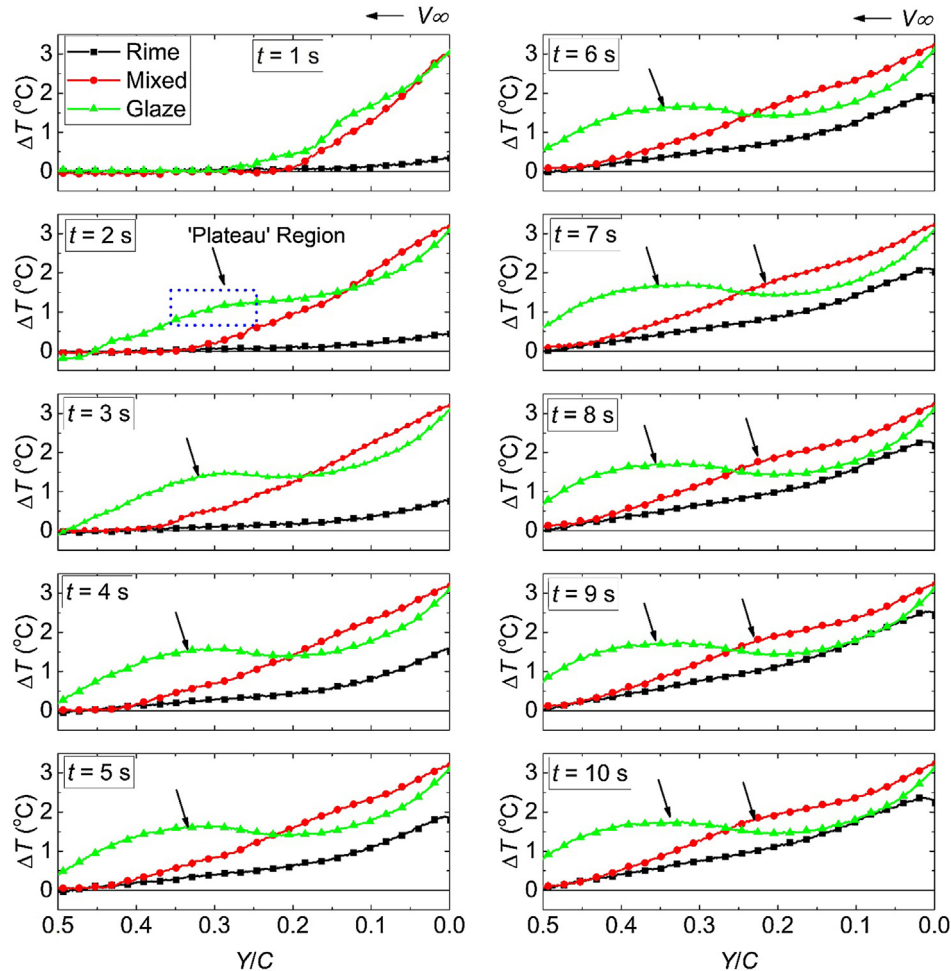


Fig. 10. Stream-wise surface temperature variations within the first 10 s under rime, mixed and glaze icing conditions.

surface water, the water film expands downstream and breaks into several isolated rivulets. The previous study has revealed the water/ice thickness distribution over the airfoil surface [14], in which the surface water/ice at $Y/C > 0.3$ is found to become thicker due to the formation of the water film/rivulets fronts. The thicker water/ice would indicate more latent heat of fusion stored locally at the surface, and hence, a higher temperature, corresponding to the temperature 'plateau' shown in Fig. 10. Compared with glaze icing condition, the 'plateau' phenomenon is not obvious in the mixed icing case due to the less runback water. However, the largest ΔT near the airfoil LE is observed in the mixed icing case, which is due to the more intensive solidification of the surface water. Similar findings are also suggested in the previous literatures [36–39], which indicates that mixed ice accretion may have more severe effects on the wind turbine performance.

6. Conclusions

An experimental study of the dynamic ice accretion process on a wind turbine blade under various icing conditions was conducted in the IRT-ISU. The test cases discussed in the present study are based on one typical ambient temperature ($-10\text{ }^{\circ}\text{C}$) and three characteristic LWC levels (i.e., 0.3 g/m^3 , 1.1 g/m^3 , 3.0 g/m^3) to duplicate rime, glaze and mixed ice conditions that wind turbines may experience in winter. The effects of centrifugal force on the icing process were estimated and evaluated by comparing with

the dominant aerodynamic force. It shows that centrifugal effects are negligible for wind turbine blade/airfoil icing, especially for the outer blade section. The full life cycle of dynamic ice accretion could be divided into two or three stages depending on the different icing morphologies. Under a glaze icing condition, there are typical three stages, including the stage of water droplet impingement and water film expansion, the later rivulet formation, and the further ice accretion along the leading edge of the airfoil model. Under a rime icing condition, there are mainly two stages: droplet impingement and continuous ice accretion. To further quantify the icing process, three icing impacted regions, i.e., (1) ice film, (2) ice rivulet and (3) ice thickness along the airfoil LE, were defined and their dimensions were calculated. Ice film lengths over the pressure-side surface of DU96-W-180 airfoil model under three icing conditions were approximately 40% C. In the glaze icing case, the accumulative length of the ice rivulet length and ice film length was approximately 80% C. Ice thicknesses along the airfoil LE would increase in a general linear trend during the dynamic ice accretion process. The ice thickness and corresponding ice growth rate were found to be smaller than the expected value under the glaze icing condition, which is mainly due to the surface water runback phenomena. Furthermore, time evolutions of stream-wise surface temperature distributions during the icing process were provided. As downstream distance from the LE increases, the surface temperature at a certain icing moment would decrease monotonously after the stagnation point in rime icing case. However,

'plateau' regions in the surface temperature distribution were observed in glaze and mixed icing cases due to the water runback phenomena.

Conflict of interest

The authors declare no conflict of interest.

Acknowledgments

This research was supported by National Science Foundation (NSF), the United States of America, under award numbers of CMMI-1824840 and CBET-1435590. The authors also want to thank Dr. Rye Waldman of Iowa State University for his help in conducting the present study.

Appendix A. Supplementary material

Supplementary data associated with this article can be found, in the online version, at <https://doi.org/10.1016/j.ijheatmasstransfer.2018.12.181>.

References

- [1] V. Lehtomäki, Wind Energy in Cold Climates Available Technologies - report, 2016.
- [2] W. Energy, C. Systems, Wind Energy Projects in Cold Climates, 2017, pp. 1–43.
- [3] F. Lamraoui, G. Fortin, J. Perron, R. Benoit, Canadian icing envelopes near the surface and its impact on wind energy assessment, *Cold Reg. Sci. Technol.* 120 (2015) 76–88, <https://doi.org/10.1016/j.coldregions.2015.09.007>.
- [4] B. Tammelin, M. Cavaliere, H. Holttinen, C. Morgan, H. Seifert, K. Säänti, Wind energy production in cold climate (WECO), ETSU Contract. Rep. W/11/00452/REP, UK DTI, 1999, pp. 1–38.
- [5] F. Lamraoui, G. Fortin, R. Benoit, J. Perron, C. Masson, Atmospheric icing impact on wind turbine production, *Cold Reg. Sci. Technol.* 100 (2014) 36–49, <https://doi.org/10.1016/j.coldregions.2013.12.008>.
- [6] C. Yin, Z. Zhang, Z. Wang, H. Guo, Numerical simulation and experimental validation of ultrasonic de-icing system for wind turbine blade, *Appl. Acoust.* 114 (2016) 19–26, <https://doi.org/10.1016/j.apacoust.2016.07.004>.
- [7] H. Seifert, Technical requirements for rotor blades operating in cold climate, in: *Proc. Boreas VI*, 2003, pp. 50–55.
- [8] H. Seifert, A. Westerhellweg, J. Kröning, Risk analysis of ice throw from wind turbines, *Pap. Present. Boreas VI*, 2003, pp. 1–9.
- [9] F. Gregorio, A. Ragni, M. Airolidi, G. Romano, PIV Investigation on airfoil with ice accretions and resulting performance degradation, *IEEE*, 2001, pp. 94–105.
- [10] R. Waldman, H. Hu, High-speed imaging to quantify the transient ice accretion process on a NACA 0012 Airfoil, in: 53rd AIAA Aerosp. Sci. Meet., 2015.
- [11] K. Zhang, T. Wei, H. Hu, An experimental investigation on the surface water transport process over an airfoil by using a digital image projection technique, *Exp. Fluids* 56 (2015) 1–16, <https://doi.org/10.1007/s00348-015-2046-z>.
- [12] R.J. Hansman, K. Yamaguchi, B. Berkowitz, M. Potapczuk, Modeling of surface roughness effects on glaze ice accretion, *J. Thermophys. Heat Transf.* 5 (1991) 54–60.
- [13] Y. Liu, H. Hu, An experimental investigation on the unsteady heat transfer process over an ice accreting airfoil surface, *Int. J. Heat Mass Transf.* 122 (2018) 707–718, <https://doi.org/10.1016/j.ijheatmasstransfer.2018.02.023>.
- [14] M.B. Bragg, G.M. Gregorek, J.D. Lee, Airfoil aerodynamics in icing conditions, *J. Aircr.* 23 (1986) 76–81, <https://doi.org/10.2514/3.45269>.
- [15] G. Fortin, J. Perron, Wind turbine icing and de-icing, in: 47th AIAA Aerosp. Sci. Meet. Incl. New Horizons Forum Aerosp. Expo. 5–8 January 2009, Orlando, Florida, 2009, p. AIAA 2009-0274.
- [16] G. Fortin, J.-L. Laforte, A. Ilinca, Heat and mass transfer during ice accretion on aircraft wings with an improved roughness model, *Int. J. Therm. Sci.* 45 (2006) 595–606, <https://doi.org/10.1016/j.ijthermalsci.2005.07.006>.
- [17] L. Gao, Y. Liu, H. Hu, Quantification of dynamic glaze icing process over an airfoil surface by using a digital image projection (DIP) technique, in: 2018 Atmos. Sp. Environ. Conf. (2018, pp. 1–13. <http://doi.org/10.2514/6.2018-3829>.
- [18] K. Zhang, H. Hu, An experimental study on the transient behavior of wind-driven water runback over a flat surface, in: 54th AIAA Aerosp. Sci. Meet., American Institute of Aeronautics and Astronautics, 2016. <http://doi.org/doi:10.2514/6.2016-1123>.
- [19] Y. Liu, H. Hu, An experimental investigation on the convective heat transfer process over an ice roughened airfoil, in: 54th AIAA Aerosp. Sci. Meet., American Institute of Aeronautics and Astronautics, 2016. <http://doi.org/doi:10.2514/6.2016-1978>.
- [20] J.F. Mandell, D.D. Samborsky, D. Miller, Effects of resin and reinforcement variations on fatigue resistance of wind turbine blades, *Adv. Wind Turbine Bl. Des. Mater.* (2013) 210–250, <https://doi.org/10.1533/9780857097286.2.210>.
- [21] W.A. Timmer, R.P.J.O.M. van Rooij, Summary of the Delft University wind turbine dedicated airfoils, *J. Sol. Energy Eng.* 125 (2003) 488, <https://doi.org/10.1115/1.1626129>.
- [22] Mikron Instrument Company, Table of Emissivity of Various Surfaces, 2014, pp. 1–13. http://www-eng.lbl.gov/~dw/projects/DW4229_LHC_detector_analysis/calculations/emissivity2.pdf.
- [23] O. Yirtici, I.H. Tuncer, S. Ozgen, Ice Accretion Prediction on Wind Turbines and Consequent Power Losses, *J. Phys. Conf. Ser.* 753 (2016) 22022, <https://doi.org/10.1088/1742-6596/753/2/022022>.
- [24] O. Agent, Task 19 Work plan 2016–2018, 2016.
- [25] Lorenzo Battisti, Gli impianti motori eolici, 2012.
- [26] L. Battisti, Wind Turbines in Cold Climates, 2015. <http://doi.org/10.1007/978-3-319-05191-8>.
- [27] Anon., FAA Federal Aviation Regulations (FAR-25), 2013.
- [28] L. Shu, H. Li, Q. Hu, X. Jiang, G. Qiu, G. McClure, H. Yang, Study of ice accretion feature and power characteristics of wind turbines at natural icing environment, *Cold Reg. Sci. Technol.* 147 (2018) 45–54, <https://doi.org/10.1016/j.coldregions.2018.01.006>.
- [29] K.M. Al-Khalil, T.G. Keith, K.J. DeWitt, Development of an anti-icing runback model, 28th Aerosp. Sci. Meet., 1990. <http://doi.org/10.2514/6.1990-759>.
- [30] R.M. Waldman, H. Li, H. Hu, An experimental investigation on the effects of surface wettability on water runback and ice accretion over an airfoil surface, in: 8th AIAA Atmos. Sp. Environ. Conf., American Institute of Aeronautics and Astronautics, Virginia, 2016. <http://doi.org/10.2514/6.2016-3139>.
- [31] Z. Jin, H. Hu, Icing process of small water droplets impinging onto a frozen cold plate, *J. Thermophys. Heat Transf.* 24 (2010) 841–845, <https://doi.org/10.2514/1.49606>.
- [32] D. Anderson, Acceptable tolerances for matching icing similarity parameters in scaling applications, in: 39th Aerosp. Sci. Meet. Exhib, 2001. <http://doi.org/10.2514/6.2001-832>.
- [33] Y. Liu, L.J. Bond, H. Hu, Ultrasonic-attenuation-based technique for ice characterization pertinent to aircraft icing phenomena, *AIAA J.* 55 (2017) 1–8, <https://doi.org/10.2514/1.J055500>.
- [34] Y. Liu, L. Li, Z. Ning, W. Tian, H. Hu, Experimental investigation on the dynamic icing process over a rotating propeller model, *J. Propuls. Power.* (2018) 1–15, <https://doi.org/10.2514/1.B36748>.
- [35] W.H. Hofmeister, R.J. Bayuzick, M.B. Robinson, Dual purpose pyrometer for temperature and solidification velocity measurement, *Rev. Sci. Instrum.* 61 (1990) 2220–2223, <https://doi.org/10.1063/1.1141393>.
- [36] S. Özgen, M. Cambek, Ice accretion simulation on multi-element airfoils using extended Messinger model, *Heat Mass Transf.* 45 (2009) 305–322, <https://doi.org/10.1007/s00231-008-0430-4>.
- [37] Y. Li, K. Tagawa, F. Feng, Q. Li, Q. He, A wind tunnel experimental study of icing on wind turbine blade airfoil, *Energy Convers. Manag.* 85 (2014) 591–595, <https://doi.org/10.1016/j.enconman.2014.05.026>.
- [38] M.O.L. Hudecz, A. Koss, H. Hansen, Ice Accretion on Wind Turbine Blades, 2014, p. 115.
- [39] Y. Han, J. Palacios, S. Schmitz, Scaled ice accretion experiments on a rotating wind turbine blade, *J. Wind Eng. Ind. Aerodyn.* 109 (2012) 55–67, <https://doi.org/10.1016/j.jweia.2012.06.001>.